Efficient approaches for the reduction in the amounts of platinum towards exhaust purification and fuel cell applications

Dr. Govindachetty Saravanan,
Department of Materials Life Chemistry
Kanagawa University
23-816, 3-27-1 Rokkakubashi, Kanagawa Ku, Yokohama 221-8686
Ph.: 045-481-5661 (Ext. 3885) e-mail: saravangchem@gmail.com

Green house gas emissions (CO, CO_2, NO_x, C_nH_n, SO_2, etc.) from fossil fuels influence seriously to the earth, so-called global warming. Most of the engine-equipped machines including generator sets, mining equipments, etc. emit these toxic gases. In the normal operation, the tailpipe emissions of a typical automobile engine exhaust are CO (0.5%), NO_x (900 ppm), C_nH_n (350 ppm), H_2 (0.17%), O_2 (0.5%), CO_2 (10%), and H_2O (10%). Enormous efforts have been spent to prevent the exhaust gas emissions in various sectors by producing of catalytic converter (Figure 1) or creation of new generation of energy, for instance fuel cells (Figure 2). Platinum group metals (PGM) (Pt, Pd, Rh) catalysts showed an outstanding catalytic behavior towards exhaust purification as well as fuel cell application due to (1) excellent thermal stability (2) less detrimental interactions with the most of the supporting materials (3) less passivity against passive materials-containing stream (4) superior activity towards the fuel conversion (5) it doesn't form any volatile oxides at harsh conditions. Although PGM catalysts possessing superior catalytic activity, however, there would be an essential need to investigate the catalysts that are containing less PGM or non-PGM due to the concerns over the cost and availability of PGM metals.

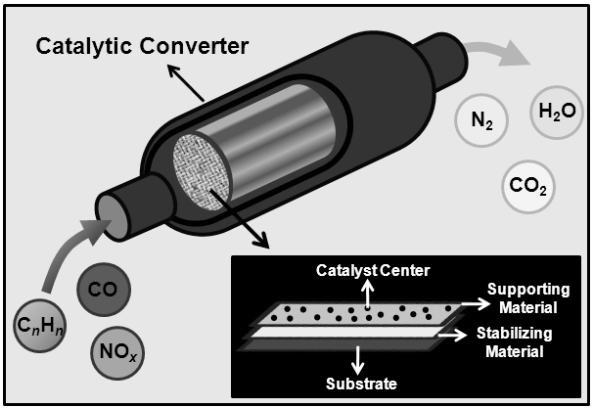

Figure 1. Schematic illustration of exhaust purification in catalytic converters.

Intermetallic nanoparticles (NPs) have drawn much attention in recent years owing to their outstanding catalytic, electronic and/or optical properties. The ever synthesized PGM-based intermetallic catalytic centers with the lower amounts of precious metals showed superior catalytic activity and lower light-off temperature in the case of exhaust purification and also showed lower onset electric potential with high current density than pure PGM in

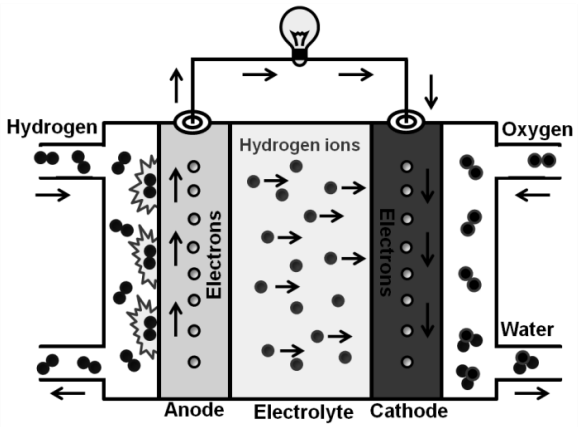

Figure 2. Schematic illustration of fuel cell.

the case of polymer electrolyte membrane fuel cells. Pt-based intermetallic NPs, in particular, Pt_3Ti NPs have taken paramount importance due to their improved catalytic performance for automotive applications The details about superior catalytic activity of Pt_3Ti NPs than pure Pt NPs towards CO oxidation and oxygen reduction reaction (ORR) would be discussed.

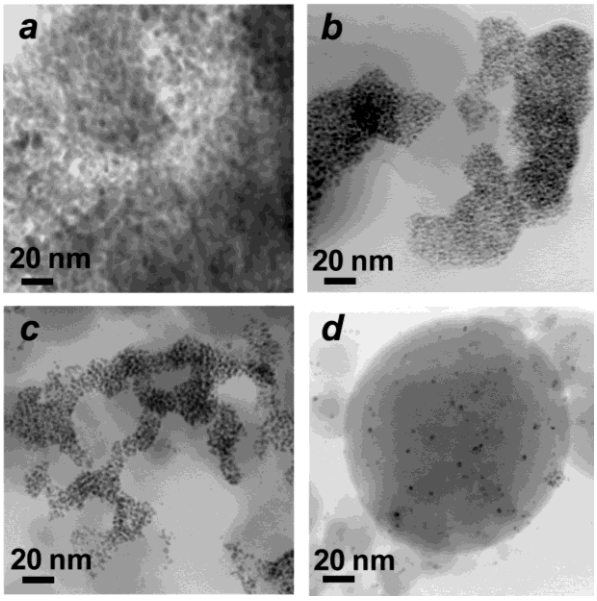

Figure 3. Bright field UHV-STEM images of free Pt_3Ti NPs (*a*) and SiO_2-supported Pt_3Ti NPs with various amounts of SiO_2 relative to Pt precursors: $x = 2$ (*b*), $x = 10$ (*c*) and $x = 50$ (*d*).

Pt_3Ti nanoparticles for CO oxidation

O_2- and moisture-free environment (< 5 ppm) is necessary to synthesize Pt_3Ti NPs because the Pt- and Ti precursors are highly air-sensitive. A precursor solution was prepared by dissolving of Pt(1,5-cyclooctadiene)Cl_2 (15.6 mg, 0.04 mmol) and $TiCl_4$(tetrahydrofuran)$_2$ (55.7 mg, 0.16 mmol) in dry tetrahydrofuran (10 ml) under a dry Ar atmosphere. Various amounts, *x*, of SiO_2 as solid supports relative to Pt precursor were added to the precursor solution. A sodium-naphthalide solution was prepared by dissolving of sodium metal (34.5 mg, 1.5 mmol) and naphthalene (192.3 mg, 1.5 mmol) in tetrahydrofuran (50 ml). The precursor/SiO_2 solution was transferred to the sodium-naphthalide solution without being exposed to air. The dark green color of sodium naphthalide turned dark brown immediately upon transfer of the precursor solutions. After overnight stirring, the solvent was removed by distillation under reduced pressure to leave a dark brown precipitate. The precipitate was washed with hexane and methanol in sequence and was dried under vacuum. The obtained products were stable in air and were black in color (free Pt_3Ti NPs and $x = 2$) or gray in color ($x = 10$ and 50).

Figure 3 presents bright field vacuum scanning transmission electron microscope (UHV-STEM) images of free Pt_3Ti NPs (Figure 3*a*) and the SiO_2-supported catalysts (Figures 3*b*-*d*). The free Pt_3Ti NPs, seen in Figure 3*a* as dark spots, agglomerate to form large clusters. Pt_3Ti NPs for $x = 2$ also form clusters adhering to the surface of SiO_2 supports which are seen in the figure as a light-colored material (Figure 3*b*). The clusters of NPs, however, become small and discrete with an increasing amount of SiO_2 (Figure 3*c*). Moreover, the distances between individual NPs increase with increasing SiO_2 amounts. Individual NPs can be clearly recognized and are finely dispersed on the surface of SiO_2 for $x = 50$ (Figure 3*d*). The particle size shows a normal distribution ranging from 1.9 to 3.1 nm and centered at 2.5 nm, regardless of the amounts of SiO_2.

Hard X-ray photoemission spectroscopy (HX-PES) measurements were performed on the SiO_2-supported Pt_3Ti NPs to ensure the formation of the intermetallic Pt_3Ti phase. Figure 4 shows HX-PES profiles in the Pt $3d_{5/2}$ region for SiO_2-supported Pt_3Ti NPs and for bulk samples of Pt and Pt_3Ti. The Pt $3d_{5/2}$ emission from the bulk Pt surface has a binding energy of 2122.2±0.05 eV. The Pt $3d_{5/2}$ binding energy for the bulk Pt_3Ti surface, 2122.5±0.05 eV, shows a chemical shift by 0.3 eV relative to that for the Pt surface. The Pt $3d_{5/2}$ binding energy for the SiO_2-supported Pt_3Ti NPs, 2122.5±0.05 eV, is consistent with the value for the Pt_3Ti surface. The Pt_3Ti NPs existed as an intermetallic Pt_3Ti phase on SiO_2 supports.

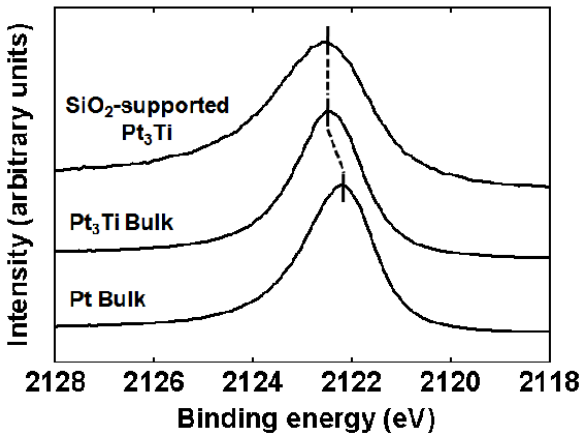

Figure 4. HX-PES spectra for SiO_2-supported Pt_3Ti NPs, Pt3Ti bulk and Pt bulk in the Pt $3d_{5/2}$ region.

Figure 5 shows catalytic CO conversion at elevated temperatures over $Pt_3Ti(0.5)/SiO_2$ and $Pt(0.5)/SiO_2$. The loading weight of Pt is represented in the parenthesis. At room temperature, neither catalysts show any evidence of CO conversion. With increasing temperature, the CO conversion over $Pt(0.5)/SiO_2$ becomes finite at an onset temperature of 200 °C and steeply grows, reaching full conversion at 325 °C. The trend of catalytic CO conversion over $Pt_3Ti(0.5)/SiO_2$ is similar, but a finite CO conversion is recognized at a lower onset temperature of 125 ºC. $Pt(0.5)/SiO_2$ showed a negligible CO conversion rate at the onset temperature of $Pt_3Ti(0.5)/SiO_2$, 125 ºC. At 225 ºC, 11.5% CO conversion was achieved by $Pt_3Ti(0.5)/SiO_2$, but only 3.9% was converted by $Pt(0.5)/SiO_2$. Full CO conversion was achieved at 300 °C by $Pt_3Ti(0.5)/SiO_2$, but for $Pt(0.5)/SiO_2$ was done at 325 °C. The inset of Figure 5 shows the CO conversion rates for $Pt_3Ti(0.5)/SiO_2$ and $Pt(0.5)/SiO_2$ at temperatures lower than 150 ºC, which are normalized to the mole amounts of Pt contained in the catalysts (mol CO (mol Pt min)$^{-1}$). The CO conversion rate for $Pt(0.5)/SiO_2$ is consistent with the reported values (Pt NPs/SiO_2, particle size 3.3 nm). The CO conversion rate for $Pt_3Ti(0.5)/SiO_2$ is higher than double the CO conversion rate for $Pt(0.5)/SiO_2$ over the entire temperature range.

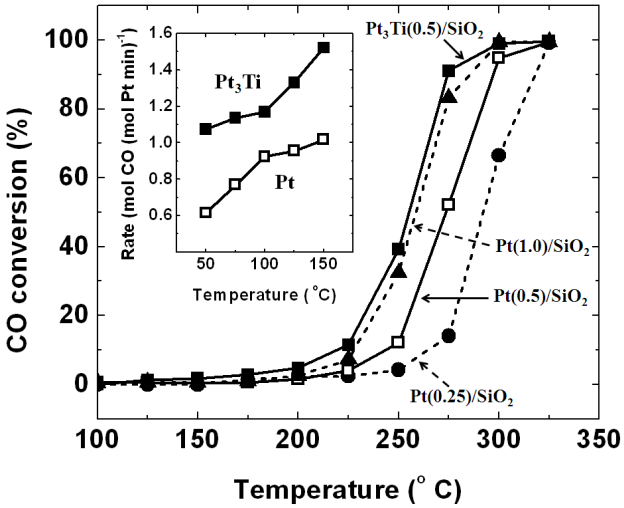

Figure 5. Temperature dependence of CO conversion over SiO_2-supported Pt_3Ti and Pt catalysts. Inset shows the temperature dependence of conversion rates for $Pt_3Ti(0.5)/SiO_2$ and $Pt(0.5)/SiO_2$.

SiO_2-supported pure Pt NPs with 0.25 (called Pt(0.25)/SiO_2 hereafter) and 1.0 wt. % of Pt (called Pt(1.0)/SiO_2 hereafter) were also synthesized using the same method as for Pt(0.5)/SiO_2. The onset temperature for Pt(0.25)/SiO_2 was 225 °C and only 66.4% CO conversion was achieved at 300 °C by this catalyst. The catalytic activity of Pt(0.25)/SiO_2 was lower than that of the Pt(0.5)/SiO_2. The onset temperature for Pt(1.0)/SiO_2 was 200 °C and 7.3% CO conversion was achieved at 225 °C by this catalyst. It is worth noting that the onset temperature for Pt(1.0)/SiO_2 was higher than that for Pt_3Ti(0.5)/SiO_2 by 75 °C. In addition, the CO conversion rate for Pt(1.0)/SiO_2 was lower than that for the Pt_3Ti(0.5)/SiO_2 at any temperature. The sizes of the catalytic NPs were the same for SiO_2-supported Pt_3Ti NPs and SiO_2-supported pure Pt NPs. The support, SiO_2, likely not affects the activity of the catalytic NPs. We conclude that Pt_3Ti NPs possess a much higher catalytic activity toward CO oxidation than pure Pt NPs. The incorporation of Ti into Pt NPs promotes enhanced catalytic activity toward CO oxidation.

Pt_3Ti nanoparticles for oxygen reduction reaction

Although Pt_3Ti NPs show superior catalytic activity than pure Pt NPs, however, as-prepared Pt_3Ti NPs are precluded from practical applications due to their agglomeration behavior. Finely dispersed Pt_3Ti NPs are anticipated to explore their superior performance for variety of applications. Finely dispersed Pt_3Ti NPs were successfully prepared from their agglomerates through an adequate post-synthesis route and demonstrated the merit of finely dispersed Pt_3Ti NPs. Generation 5, poly(amidoamine) (PAMAM) dendrimers (G5OH) was utilized to disperse Pt_3Ti NPs. Intermetallic Pt_3Ti NPs (1.0 - 4.0 nm) were first synthesized and used as a starting material for the synthesis of Pt_3Ti@G5OH. An aliquot of Pt_3Ti NPs (5 mg) was mixed with dendrimer solutions (5 ml, 0.2 mM) and stirred for 8 days at room temperature. After stirring, these solutions were centrifuged at 6000 rpm for 30 min. The resulting supernatant was a transparent, brown solution. Similarly, generation 2, PAMAM dendrimers (G2OH) was used to disperse Pt_3Ti NPs.

The structure of Pt_3Ti@G5OH was determined by HX-PES as shown in Figure 6. Pt $3d_{5/2}$ emission from as-prepared Pt_3Ti NPs had a binding energy of 2122.5±0.2 eV, consistently with Pt_3Ti bulk. The Pt_3Ti NPs, which were dispersed in an aqueous solution of G2OH (Pt_3Ti/G2OH), showed a Pt $3d_{5/2}$ binding energy of 2122.7±0.2 eV. The Pt $3d_{5/2}$ binding energy for Pt_3Ti@G5OH, however, was shifted by 2.2 eV toward higher energies relative to Pt_3Ti/G2OH, as-

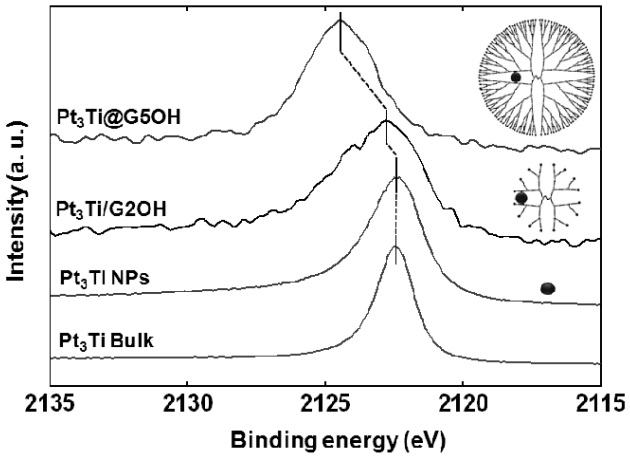

Figure 6. HX-PES spectra in the Pt $3d_{5/2}$ region for Pt_3Ti bulk, as-prepared Pt_3Ti NPs, Pt_3Ti/G2OH and Pt_3Ti@G5OH.

prepared Pt_3Ti NPs, and Pt_3Ti bulk. It is known that photoemission from metal NPs or clusters, when their surfaces are covered with insulating layers of atomic thickness, exhibits a larger binding energy owing to slow neutralization of holes (final-state effect). The large Pt $3d_{5/2}$ binding energy of Pt_3Ti@G5OH is interpreted as a final-state effect on the Pt_3Ti NPs, which were surrounded by the insulating pore of G5OH. No final-state effect was recognized for Pt_3Ti/G2OH because the Pt_3Ti NPs were not fully enveloped in the incomplete pores of G2OH.

Figure 7*a* shows a high-angle annular-dark-field transmission electron microscopy (HAADF-TEM) image of as-prepared Pt_3Ti NPs. The Pt_3Ti NPs, observed as bright spots, were highly agglomerated, and their particle size showed a normal distribution centered at 2.5 nm ranging from 1.0 to 4.0 nm (inset). Figure 7*b* shows a HAADF-TEM image of Pt_3Ti@G5OH. The metal cores of Pt_3Ti@G5OH are observed as bright spots. The size of the Pt_3Ti NPs, evaluated from this HAADF-TEM image, showed an asymmetrical distribution around a maximum of 1.6 nm, ranging from 1.1 to 1.7 nm (inset). Only Pt_3Ti NPs smaller than 1.7 nm were selectively included by G5OH to form Pt_3Ti@G5OH.

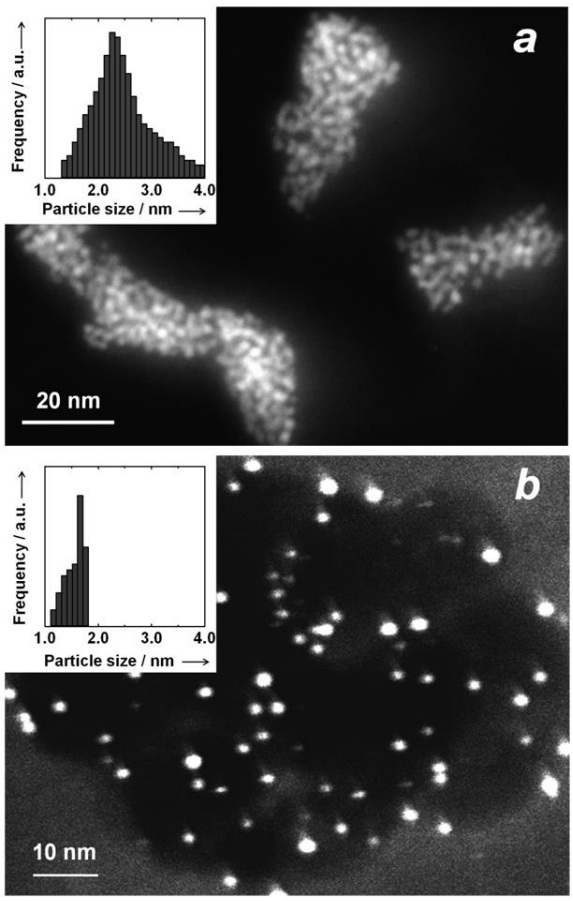

Figure 7. HAADF-TEM images of as-prepared Pt_3Ti NPs (*a*) and Pt_3Ti@G5OH (*b*). Histograms for the size of the metal NPs are shown in the insets.

Pt_3Ti@G5OH and G5OH were dispersed and immobilized on the surface of a glassy-carbon (GC) electrode by sweeping the electrode potential between 0 and +1.0 V (vs. Ag/AgCl (3 M NaCl)) at 10 mVs^{-1} in $LiClO_4$ solution. Figure 8*a* shows cyclic voltammograms for the bare GC electrode, G5OH and Pt_3Ti@G5OH acquired at a sweep rate of 10 mVs^{-1} in O_2 saturated aqueous solution of H_2SO_4 (0.5 M). The onset- and half-wave ORR potentials for the GC electrode were -0.01 V and -0.45 V, respectively. The onset- and half-wave ORR potentials of G5OH were -0.01 V and -0.45 V, respectively, indicating that G5OH is not active toward the ORR. Both the onset- and half-wave potentials for Pt_3Ti@G5OH shifted substantially toward higher potentials by 0.41 and 0.32 V, respectively, owing to the inherent activity of the incorporated Pt_3Ti NPs. The ORR activity of as-prepared Pt_3Ti NPs that were dispersed on the GC electrode with Nafion was examined under the same measurement conditions as Pt_3Ti@G5OH (Figure 8*b*). The ORR currents for as-prepared Pt_3Ti NPs

and Pt_3Ti@G5OH were normalized to the Pt loading weight. The ORR current at -0.15 V for Pt_3Ti@G5OH was 15-fold greater than that for the as-prepared Pt_3Ti NPs. The poor activity of as-prepared Pt_3Ti NPs is most likely ascribed to particle agglomeration, which diminishes the effective surface area. Pt_3Ti@G5OH exhibited a much superior ORR activity because individual Pt_3Ti NPs were encapsulated by G5OH and finely dispersed over the electrode surface.

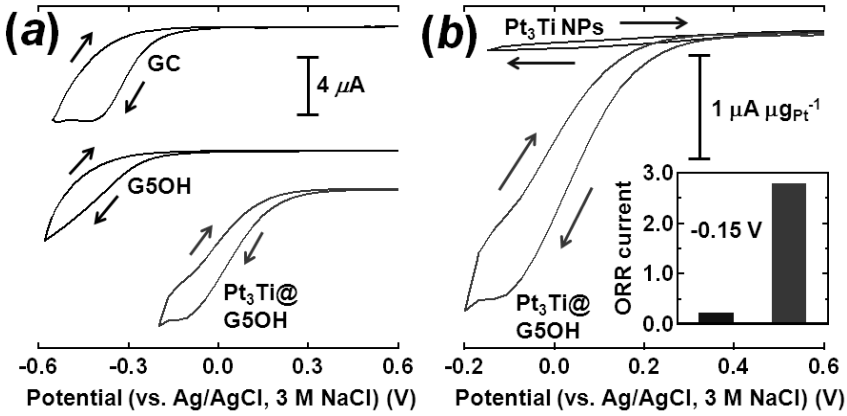

Figure 8. (*a*) Cyclic voltammograms for the ORR over a bare GC, G5OH and Pt_3Ti@G5OH. (*b*) Cyclic voltammograms for the ORR over as-prepared Pt_3Ti NPs and Pt_3Ti@G5OH. Inset shows the ORR currents at -0.15 V for as-prepared Pt_3Ti NPs

In conclusion, SiO_2-supported Pt_3Ti NPs catalyst showed a higher catalytic activity toward CO oxidation than SiO_2-supported Pt NPs catalyst containing a two-fold more amount of Pt. SiO_2-supported Pt_3Ti NPs catalysts were not deactivated during catalytic oxidation of CO at elevated temperatures. Pt_3Ti NPs have promise as a catalytic center for the purification of automobile exhaust in terms of their high catalytic activity toward CO oxidation and relatively low content of precious metals. We successfully dispersed and solubilized Pt_3Ti NPs in water using the PAMAM dendrimer, G5OH as a post-synthesis surfactant. The strong interaction between the Pt_3Ti surface and the carbonyl groups on the pore surface resulted in the formation of a water-soluble nanocomposite, Pt_3Ti@G5OH. Pt_3Ti@G5OH exhibited superior ORR activity compared to agglomerated, as-prepared Pt_3Ti NPs. The post-synthesis dispersion with PAMAM dendrimers might be applicable to various kinds of functional NPs and will strongly prompt their applications to PEFCs and/or fluorescent imaging.

References

1. Abe, H.; Matsumoto, F.; Alden, L. R.; Warren, S. C.; Abruña, D. H.; DiSalvo, F. J. *J. Am. Chem. Soc*. **2008**, *130*, 5452-5458.

2. Saravanan, G.; Abe, H.; Xu, Y.; Sekido, N.; Hirata, H.; Matsumoto, S-I.; Yoshikawa, H.; Yamaba-Mitarai, Y. *Langmuir*, **2010**, *26*, 11446-11451.

3. Saravanan, G.; Hara, T.; Yoshikawa, H.; Yamashita, Y.; Ueda, S.; Kobayashi, K.; Abe, H. *Chem. Commun*., **2012**, *48*, 7441–7443.